batteries

MDPI

Article

Prediction of the Remaining Useful Life of Lithium-Ion Batteries Based on Health Features Extraction and Improved Stochastic Configuration Networks

Xinlu Wang [1], Zhijun Gao [2,*], Xifeng Guo [2], Yi Ning [2] and Yiyang Liu [2]

[1] School of Mechanical Engineering, Shenyang Jianzhu University, Shenyang 110168, China; wangxinlu06@stu.sjzu.edu.cn
[2] School of Electrical and Control Engineering, Shenyang Jianzhu University, Shenyang 110168, China; guoxifeng@sjzu.edu.cn (X.G.); vipningyi@sjzu.edu.cn (Y.N.); liuyy@stu.sjzu.edu.cn (Y.L.)
* Correspondence: gzj@sjzu.edu.cn

Abstract

The remaining useful life (RUL) of lithium-ion batteries plays a crucial role in fault prognosis and health management. Therefore, accurate RUL prediction can effectively improve equipment safety and mitigate operational risks. However, existing RUL prediction methods often exhibit limited accuracy caused by capacity regeneration and excessively long training times due to model complexity. In this study, Pearson and Spearman correlation analyses are employed to effectively extract health features that are highly correlated with battery capacity to characterize capacity degradation, and a lithium-ion battery RUL prediction model based on stochastic configuration networks (SCNs) optimized by sparrow search algorithm (SSA) is proposed. The battery datasets from NASA and CALCE are used for validation and testing. Experimental results demonstrate that the proposed SSA-SCN achieves a root mean squared error of 0.0036 and a mean absolute error of 0.0030, while exhibiting faster training time compared with other hybrid methods. The results verify that the proposed method can provide more accurate battery RUL predictions and effectively improve the accuracy and reliability of lithium-ion battery RUL estimation.

Keywords: lithium-ion battery; remaining useful life; health features; sparrow search algorithm; stochastic configured networks

1. Introduction

The depletion of fossil fuel reserves and the escalating impacts of climate change have posed significant challenges to the sustainable development of renewable energy, smart grids, and clean transportation systems. Owing to their advantages of high energy density, low self-discharge, environmental friendliness, and long service life, lithium-ion batteries have been widely applied in these fields and play an important role [1–3]. However, with repeated charge–discharge cycles during operation, numerous electrochemical side reactions continuously occur in the anode, electrolyte, and cathode, leading to progressive performance degradation of the battery. Consequently, the remaining useful life (RUL) of the battery degrades [4], significantly impairing charge–discharge performance and potentially leading to malfunction or even safety accidents under extreme conditions. Accurate prediction of battery RUL can provide critical guidance for preventive maintenance and safe, stable operation, reduce maintenance costs, and mitigate the risk of catastrophic failures [5].

Check for updates

Academic Editor: Diego Iannuzzi

Received: 31 January 2026
Revised: 25 February 2026
Accepted: 27 February 2026
Published: 26 March 2026

Copyright: © 2026 by the authors. Licensee MDPI, Basel, Switzerland. This article is an open access article distributed under the terms and conditions of the Creative Commons Attribution (CC BY) license.

As a core function of the battery management system (BMS), remaining useful life (RUL) prediction has attracted increasing attention in recent years [6], as it aims to estimate the remaining number of charge–discharge cycles before the battery reaches the failure threshold (FT) under its current health state and nominal operating conditions [7]. Currently, existing battery RUL prediction techniques can be broadly categorized into model-based methods and data-driven methods [8,9].

Model-based prediction methods utilize mathematical models that characterize battery aging behavior to examine the relationship between performance degradation and aging-related performance indicators [10]. Equivalent circuit model-based approaches are unable to fully capture the dynamic variations in batteries [11]. Electrochemical models are established on the basis of reaction mechanisms during electrochemical processes; however, due to the excessive complexity of internal battery reactions, it is difficult to construct accurate degradation models [12]. Consequently, model-based estimation methods remain challenging and generally exhibit limited prediction accuracy [13]. In contrast, data-driven methods can effectively avoid the aforementioned problems.

Data-driven methods do not require consideration of the internal physicochemical reaction processes of batteries and directly use historical monitoring data to predict battery degradation trends, such methods mostly adopt machine learning algorithms [14,15]. Sun et al. [16] proposed a modeling strategy that decomposes the degradation process into analyzable stages and employed support vector machines (SVMs) to predict lithium-ion battery capacity degradation. In addition to machine learning approaches, statistical analysis methods under a probabilistic framework are also commonly used for RUL prediction in data-driven methods [17], including Gaussian process regression [18] and sample entropy-based statistical methods [19]. With the development of artificial intelligence, deep learning-based RUL prediction methods have attracted increasing attention [20]. In ref. [21], high SOH prediction accuracy was achieved by integrating an improved gray wolf optimization algorithm with a deep extreme learning machine; however, the method relies on manual feature extraction. Ref. [22] significantly improved SOH prediction accuracy by constructing an activation function library and adaptively enabling long short-term memory (LSTM) to select more suitable activation functions at different stages. However, the method relies on empirical rules for activation function selection. Ref. [23] achieved accurate and interpretable RUL prediction by combining bidirectional long short-term memory (BiLSTM) and Transformer with a knee-point initiation strategy; however, the model has a complex structure and was mainly validated on a single battery, leaving its cross-battery generalization capability to be further evaluated.

The raw capacity sequence of batteries often exhibits pronounced non-stationarity and is coupled with capacity regeneration, measurement noise, and multi-scale degradation characteristics, which limits the model's ability to effectively learn the true degradation patterns [24]. Ref. [25] integrated variational mode decomposition (VMD), an attention mechanism, and temporal convolutional network (TCN) to effectively separate high-frequency noise and enhance long-term sequence modeling capability. Ref. [26] decomposed the capacity sequence using complete ensemble empirical mode decomposition with adaptive noise (CEEMDAN) and combined it with parallel BiLSTM to effectively characterize multi-scale degradation features and capacity regeneration, significantly improving the stability of RUL prediction. Ref. [27] targeted small-sample scenarios by integrating CEEMDAN and principle component analysis feature enhancement and achieved high accuracy RUL prediction using only 10% of the data. However, the use of VMD and CEEMDAN increases computational complexity and parameter tuning cost and may easily lead to data leakage. To address the problems of insufficient generalization and lack of physical consistency under small-sample and varying operating conditions, recent studies have

introduced physical information into models to enhance interpretability, robustness, and cross-condition prediction capability while retaining the high representational power of data-driven methods [28]. Ref. [29] introduced empirical degradation models and physical constraints into a data-driven framework using physics-informed neural networks, achieving high stability and a certain level of interpretability under small-sample, cross-battery, and cross-condition scenarios. Ref. [30] achieved label-free, small-sample RUL prediction with strong interpretability by relying solely on online capacity data of a single battery using Kalman filter and Wiener degradation model; however, the simplified model assumptions and reliance on a single capacity feature require further validation for real-time applications.

Compared with pure data-driven methods, model-based methods based on identification have also received extensive attention in recent years. Such methods typically identify and update model parameters on the basis of a pre-defined model structure through techniques such as least squares or swarm intelligence optimization [31]. Reference [32] proposes a SOH estimation method based on impulse response and temperature-extended ARX models, achieving joint estimation of battery capacity degradation and internal resistance increase. This method significantly improves the accuracy and trend tracking ability of SOH estimation under different temperature conditions and has a relatively low computational complexity suitable for real-time implementation in BMS. Reference [33] focuses on the swarm intelligence and meta-heuristic optimization identification of ECM parameters, treating the identification as a global optimization problem, which is suitable for parameter identification scenarios with non-convex cost functions, initial value sensitivity, or numerous local minima. However, model-based methods based on identification rely on pre-defined model structures, and their modeling capabilities are limited by model order and structural assumptions. Additionally, the parameter identification process is sensitive to the quality of the excitation signal and noise level, which can lead to parameter drift or unstable identification. Therefore, enhancing the model's ability to express complex degradation behaviors remains an important issue that needs to be further addressed for identification-based models.

Based on the above analysis, this study extracts characteristic parameters of lithium-ion batteries as health features (HFs) and proposes a stochastic configuration network (SCN) model optimized by the sparrow search algorithm (SSA), thereby constructing HFs and SSA-SCN-based prediction method. The proposed method is validated using the NASA and the CALCE battery datasets, and the experimental results demonstrate that the proposed method achieves superior accuracy and robustness in RUL prediction.

The organization of this paper is as follows: Section 2 describes the lithium-ion battery datasets used in the experiments and presents the extraction of HFs, and Section 3 introduces the related algorithms and constructs the SSA-SCN method for RUL prediction. Section 4 provides an experimental validation of the proposed method and compares its prediction performance with that of classical approaches. Finally, Section 5 concludes the paper.

2. Health Features of Lithium-Ion Batteries

2.1. Dataset of Lithium-Ion Batteries

The data used in this study are obtained from the first dataset released by the National Aeronautics and Space Administration Prognostics Center of Excellence (NASA PCoE) [34], which consists of aging data for 18650 lithium cobalt oxide batteries with a nominal capacity of 2 A·h, including cells B0005, B0006, B0007, and B0018. The batteries are subjected to repeated charge and discharge cycling tests, and each cycle consists of a charging stage and a discharging stage. Specifically, during charging, the lithium-ion battery is first charged

under a constant current of 1.5 A until the voltage reaches 4.2 V and then charged at a constant voltage of 4.2 V until the current decreases to 20 mA. During discharging, the battery is discharged at a constant current of 2 A until the voltage reaches a predefined cut-off value. The charge and discharge cycle is illustrated in Figure 1.

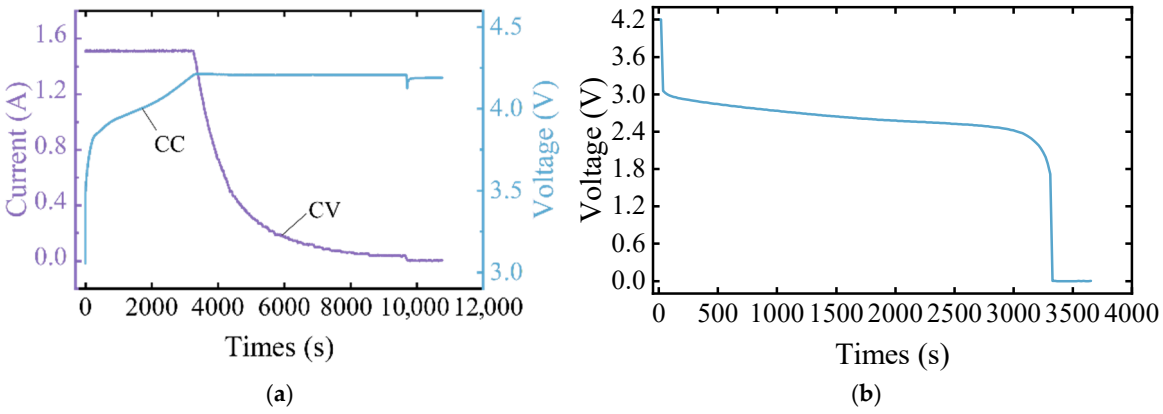


Figure 1. Current and voltage variation curves during the cycle. (**a**) Current and voltage variation in charging stage. (**b**) Voltage variation in discharging stage.

The capacity degradation curves of the four lithium-ion batteries used in the experiments are shown in Figure 2. In the NASA dataset, battery capacity regeneration is observed during the aging process. According to international standards for lithium-ion battery performance testing, batteries are required to operate normally at room temperature, and a battery is considered to have failed when its actual capacity drops to 70–80% of the rated capacity, at which point replacement is required to ensure system safety and reliability. In the description files of the NASA dataset, the battery FT is defined as 70% capacity. Therefore, the FT of B0005, B0006, and B0018 is set to 1.4 A·h, while for B0007, whose capacity does not decrease to 1.4 A·h, 1.45 A·h is selected as its FT.

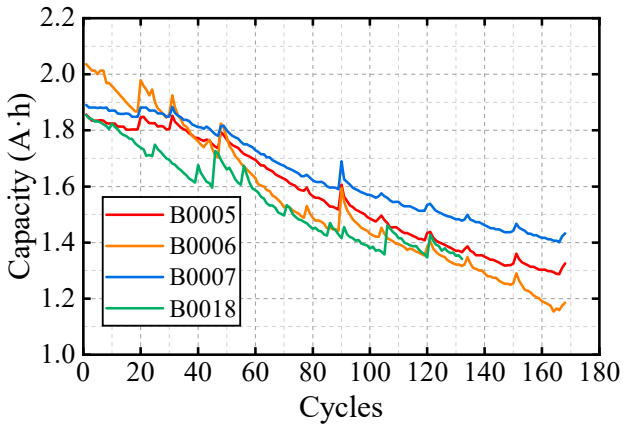


Figure 2. NASA battery capacity degradation curve.

The experimental dataset parameters include ambient temperature (AT), constant charging current (CC), charging cut-off voltage (CV), discharging current (DC), discharging cut-off voltage (DV), and FT. The detailed settings are listed in Table 1.

Table 1. Parameter information of the experimental datasets.

Battery	AT/°C	CC/A	CV/V	DC/A	DV/V	FT/(A·h)
B0005	24	1.5	4.2	2	2.7	1.4
B0006	24	1.5	4.2	2	2.5	1.4
B0007	24	1.5	4.2	2	2.2	1.45
B0018	24	1.5	4.2	2	2.5	1.4

2.2. Health Features Extraction

During electrical degradation, capacity can directly indicate the degree of battery aging. Considering the full life cycle of lithium-ion batteries, HFs extracted from variations in voltage, current, and temperature can indirectly reflect battery aging. As lithium-ion batteries undergo repeated cycling, the total charging and discharging time gradually decreases, meaning that the combined duration of CC stage and CV stage shortens as the battery ages. Taking B0005 as an example, the voltage variation curves during constant current charging and the current variation curves during constant voltage charging are extracted for the 2-nd, 50-th, 100-th, and 150-th cycles, as shown in Figure 3, and as battery degradation becomes more severe, the discharging time and the time required to reach full charge decrease; thus, charging and discharging durations can be considered as battery HFs. By examining the current and voltage data, as shown in Figure 4, an abnormal voltage charging curve is observed for B0006 at the 12-th cycle, which deviates significantly from those observed in other cycles.

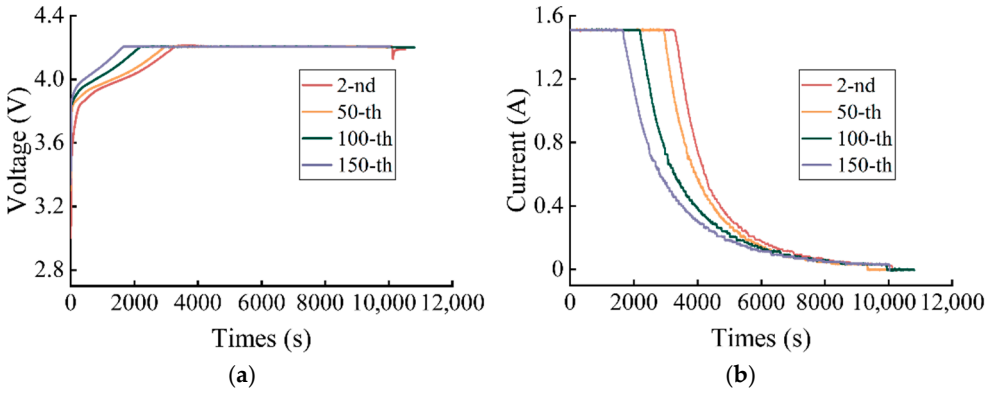


Figure 3. Time variation curves of current and voltage during charging process. (**a**) Voltage variation in CC charging. (**b**) Current variation in CV charging.

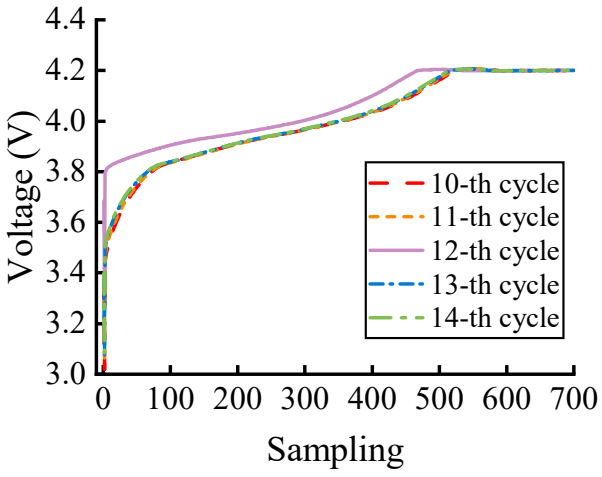


Figure 4. Abnormal voltage pattern of B0006 during its 12-th cycle.

With the increase in cycle number, the active materials inside the battery are continuously consumed, leading to a gradual decline in reversible charge and discharge capability and a continuous increase in internal resistance, which results in capacity degradation. As the cycle number increases, battery performance inevitably degrades, regardless of external operating conditions or detailed knowledge of internal physicochemical reactions. Therefore, the cycle number is selected as the first health feature to characterize battery health status and is denoted as HF1.

To verify the feasibility of the extracted health features and further quantify the degree of correlation between HFs and capacity, Pearson and Spearman correlation analysis methods are employed to analyze their relationships with capacity. Given two variables $\alpha = (\alpha_1, \alpha_2, \ldots, \alpha_n)$ and $\beta = (\beta_1, \beta_2, \ldots, \beta_n)$, Pearson correlation coefficient r_p can be expressed as:

$$r_p = \frac{E(\alpha\beta) - E(\alpha)E(\beta)}{\sqrt{E(\alpha)^2 - (E(\alpha))^2}\sqrt{E(\beta)^2 - (E(\beta))^2}} \quad (1)$$

where E denotes the expectation value. When the two vectors exhibit a very strong linear relationship, the correlation coefficient approaches -1 or 1. If the two variables are independent of each other, the Pearson correlation $r_p = 0$.

Spearman correlation coefficient r_s can be expressed as:

$$r_s = \frac{\sum_i (\alpha_i - \overline{\alpha})(\beta_i - \overline{\beta})}{\sqrt{\sum_i (\alpha_i - \overline{\alpha})^2 \sum_i (\beta_i - \overline{\beta})^2}} \quad (2)$$

where α and β denote the mean values of α and β, respectively, and r_s ranges from -1 to 1.

Pearson and Spearman correlation coefficients can be used to evaluate the correlation between two variables [35]. The magnitude of the absolute value reflects the strength of the correlation. When the absolute value equals 1, the two variables are perfectly correlated. When the variables are continuous, follow a normal distribution, and exhibit a linear relationship, Pearson correlation coefficient is most appropriate, otherwise, Spearman correlation coefficient is more efficient. Accordingly, both Pearson and Spearman coefficients are jointly used to perform comprehensive selection of HFs.

The battery discharging process can be divided into three stages, namely a rapid voltage drop stage, a discharge plateau stage, and a sharp voltage decline stage. In the first stage, the voltage rapidly decreases from approximately 4.2 V to 4.0 V. In the second stage, it gradually decreases from about 4.0 V to 3.2 V, and in the third stage, it rapidly drops to the cut-off voltage. During the second stage, the discharge voltage of the lithium-ion battery remains relatively stable and is easier to analyze, and the discharge duration is longer. Therefore, data from the second stage are selected as HF.

To obtain voltage drop information that best represents the degradation state of lithium-ion batteries, the second stage of the discharge voltage curve is adopted, and the variation in discharge time corresponding to different voltage drop ranges from 4 V to 3.2 V is investigated. With a voltage drop of 0.1 V taken as the reference, r_p and r_s between the discharge time difference and the capacity sequence, are listed in Table 2.

Table 2. Correlation analysis of equal voltage drop during the discharging stage.

	B0005		B0006		B0007		B0018	
(V)	r_p	r_s	r_p	r_s	r_p	r_s	r_p	r_s
4.0–3.9	0.9651	0.9370	0.9645	0.9610	0.9734	0.9522	0.9486	0.9350
3.9–3.8	0.9860	0.9650	0.9800	0.9880	0.9720	0.9652	0.9712	0.9724
3.8–3.7	0.9729	0.9895	0.9931	0.9972	0.9734	0.9860	0.9750	0.9786
3.7–3.6	0.9955	0.9934	0.9921	0.9969	0.9962	0.9926	0.9967	0.9933
3.6–3.5	0.9973	0.9908	0.9873	0.9982	0.9920	0.9795	0.9968	0.9955
3.5–3.4	0.9739	0.9652	0.9828	0.9919	0.9528	0.9793	0.9812	0.9863
3.4–3.3	−0.9915	−0.9780	−0.7324	−0.4863	−0.9671	−0.9625	−0.9752	−0.9598
3.3–3.2	−0.9668	−0.9625	−0.9713	−0.9698	−0.9264	−0.9289	−0.9523	−0.9726

Taking 4.0 V to 3.9 V interval as an example, during each discharge process, the time at which the voltage first reaches 4.0 V, corresponding to the upper bound of the equal voltage drop $V_{\max}$, is denoted as $t_{v\max}$, and the time at which the discharge voltage first reaches 3.9 V, corresponding to the lower bound $V_{\min}$, is denoted as $t_{v\min}$; according to Equation (3), the equal voltage drop time is calculated and used as HF.

$$t(\mathrm{HF}) = t_{v\min} - t_{v\max} \tag{3}$$

As shown in Table 2, the discharge times corresponding to voltage drops of 3.7 V to 3.6 V, 3.6 V to 3.5 V, and 3.5 V to 3.4 V exhibit high correlation coefficients with battery capacity. By examining different voltage drop ranges, it is observed that for any selected range, a larger voltage drop corresponds to a longer discharge time and a stronger correlation with capacity degradation. Within the 0.3 V voltage drop range from 3.7 V to 3.4 V, the discharge time shows the highest correlation and is therefore defined as health feature HF2.

To comprehensively analyze the degradation state of lithium-ion batteries, experiments are conducted using multiple voltage ranges as examples. Similar to the analysis of equal voltage drop discharge time, health features can also be extracted from the charging process by selecting the charging time intervals during the constant current charging stage and the constant voltage charging stage, namely the equal voltage rise stage and the equal current decrease stage. Table 3 presents the correlation analysis of equal voltage rise charging time for B0005. Based on the correlation results, the equal voltage rise charging time required for the voltage to increase from 3.8 V to 4.2 V during the constant current stage is selected as HF to characterize battery health status and is denoted as HF3.

Table 3. Correlation analysis of equal voltage rise during the constant current charging stage.

	r_p	r_s
3.8 V–4.1 V	0.9951	0.9893
3.8 V–4.2 V	0.9949	0.9910
3.9 V–4.1 V	0.9920	0.9863
3.9 V–4.2 V	0.9903	0.9856

Similarly, the charging time required for the current to decrease from 1.5 A to 0.5 A during the constant voltage stage is taken as another health feature to characterize battery health status and is denoted as HF4. Based on the above correlation analysis results, the final four health features (HF1–HF4) that have a high correlation with the capacity degradation trend will be selected as the input variables for the RUL prediction model of lithium-ion batteries. The correlations of the four HFs are shown in Table 4. From the perspective of physical mechanisms, the HF1–HF4 selected in this paper are all closely

related to the electrochemical degradation process of lithium-ion batteries. HF1 reflects the irreversible aging effect caused by the accumulation of side reactions during the cycling process; HF2 corresponds to the change in the duration of the discharge platform interval, which can characterize the influence of enhanced polarization and increased internal resistance on the discharge kinetics; HF3 reflects the voltage response characteristics during the constant current charging stage, which is closely related to the increase in impedance; HF4 characterizes the current decay process during the constant voltage stage, which can reflect the changes in charge transfer and lithium-ion diffusion capabilities. Therefore, the selected health features not only have significant statistical correlations but also have clear electrochemical physical meanings, thereby enhancing the interpretability and physical consistency of the proposed RUL prediction framework.

Table 4. Correlation analysis results between HFs and capacity.

	B0005		**B0006**		**B0007**		**B0018**	
	r_p	r_s	r_p	r_s	r_p	r_s	r_p	r_s
HF1	−0.988	−0.991	−0.982	−0.993	−0.988	−0.993	−0.970	−0.973
HF2	0.999	0.999	0.993	0.999	0.995	0.995	0.996	0.997
HF3	0.995	0.991	0.990	0.994	0.986	0.988	0.989	0.978
HF4	−0.987	−0.986	−0.940	−0.956	−0.913	−0.897	−0.798	−0.850

3. Methodology

3.1. Stochastic Configuration Networks

SCNs constitute a class of randomized machine learning algorithms [36]. Similar to other randomized learning methods, such as random weight feedforward neural networks and random vector functional link networks, SCNs randomly assign the input weights ω and biases b of hidden layer nodes and subsequently compute the output weights using regularized techniques such as least squares. Compared with other deep structured networks, SCN architecture does not involve coupling between layers. Since there is no need for interconnections among multiple layers, SCN has advantages over gradient-based layer by layer training methods that rely on backpropagation, in terms of network complexity, training speed, and parameter scale, thereby improving learning capability and computational efficiency. When network accuracy does not meet the specified requirements, the accuracy can be improved by increasing the number of hidden layer nodes. The additional computational cost incurred by increasing the number of hidden layer nodes is significantly lower than that associated with increasing network depth in conventional models. Therefore, SCN is particularly suitable for systems with limited feature dimensions that require real-time prediction.

When configuring and computing hidden layer nodes, SCN introduces a supervised mechanism and adopts an incremental learning strategy in which random parameters are assigned under inequality constraints. Starting from a simple network structure, the number of hidden layer nodes is increased according to the complexity of the training samples, the parameter ranges are adaptively adjusted, and the output weights of the nodes are computed using the least squares method to ensure good universal approximation capability. The structure of the SCN is shown in Figure 5. The algorithmic principle and universal approximation property of SCN can be described as follows:

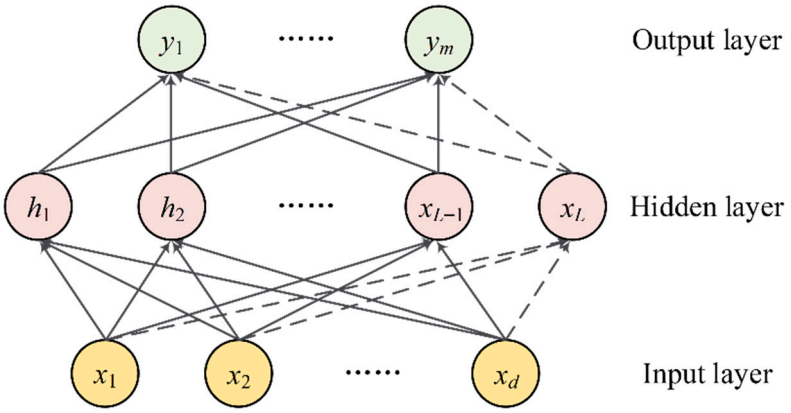


Figure 5. Structure of stochastic configuration networks.

For a given training dataset $\{X, Y\}$, $X = \{x_1, x_2, \ldots, x_n\}$ denotes the input variables, where $x_i = \{x_{i,1}, x_{i,2}, \ldots, x_{i,d}\} \in \mathrm{R}^d$, $Y = \{y_1, y_2, \ldots, y_n\}$ denotes the corresponding output variables, where $y_i = \{y_{i,1}, y_{i,2}, \ldots, y_{i,m}\}$, $i = 1, 2, \ldots, n$.

Given a target function f: $\mathrm{R}^d \rightarrow \mathrm{R}^m$, assuming that the hidden layer of SCN has generated $L-1$ nodes, the current network output can be expressed as:

$$f_{L-1}(X) = \sum_{j=1}^{L-1} \beta_j g_j(\omega_j X + b_j),\ L = 1, 2, \cdots, L_{\max},\ f_0 = 0 \tag{4}$$

where β_j denotes the output weight of the j-th node in the hidden layer. $g(\cdot)$ denotes the activation function. ω_j and b_j are the input weight and bias of the j-th hidden node, respectively, with $j = 1, 2, \ldots, L_{\max}$.

The current residual vector of the network is calculated as:

$$e_{L-1} = f - f_{L-1}(X) = [e_{L-1,1}(X), e_{L-1,2}(X), \cdots, e_{L-1,m}(X)]^T \in R^{N \times m} \tag{5}$$

If the magnitude of $\|e_{L-1}\|^2$ does not reach the predefined error ε or the number of network nodes has not reached the maximum value $L_{\max}$, the L-th hidden layer node is added, and its input weights and bias are determined according to the supervised mechanism given in Equation (7):

$$h_L = \left[g_L\left(\omega_L^T x_1 + b_L\right), g_L\left(\omega_L^T x_2 + b_L\right), \cdots, g_L\left(\omega_L^T x_N + b_L\right)\right]^T \in R^N \tag{6}$$

$$\xi_{L,q} = \frac{\left(e_{L-1}^T \cdot h_L\right)^2}{h_L^T h_L} - (1 - r - \mu_L)\left\|e_{L-1,q}\right\|^2 \tag{7}$$

where $q = 1, 2, \ldots, m$, h_L denotes the output of the L-th hidden layer node. ω_L and b_L represent the candidate input weight and bias of the L-th hidden node, respectively. $R \in (0, 1)$, $\{\mu_L\}$ denotes a sequence of non-negative real numbers, where $\mu_L \leq 1 - r$ and $lim_{\,L \rightarrow +\infty}\, \mu_L = 0$. The candidate parameters that maximize $\xi_L = \sum_{q=1}^{m} \xi_{L,q} \geq 0$ criterion are chosen as the parameters of the L-th node in the network.

The output weights of the hidden layer nodes are solved using Equation (8):

$$\beta = \underset{\beta}{\operatorname{argmin}} \|H\beta - Y\|^2 = H^+ Y \tag{8}$$

where H^+ denotes the Moore–Penrose generalized inverse of H, $H = [h_1, h_2, \ldots, h_L]$.

The network output f is expressed as:

$$f = H\beta \tag{9}$$

Assuming that $\Gamma = \{g_1, g_2, \ldots\}$ denotes a set of real valued functions, span(Γ) represents the function space spanned by Γ; span(Γ) is dense in the L_2 space, and for $\forall g \in \Gamma, 0 < \|g\| < b_g, b_g \in R^+$. If the random basis function g_L satisfies the inequality constraint:

$$\langle e_{L-1,q}, g_L \rangle^2 \geq {b_g}^2 \delta_{L,q}, \; q = 1, 2, \cdots, m \tag{10}$$

The output weights of the hidden layer nodes are expressed as:

$$\beta = [\beta_1, \beta_2, \cdots, \beta_L] = \underset{\beta}{\operatorname{argmin}} ||f - \sum_{j=1}^{L} \beta_j g_j|| \tag{11}$$

Then, $lim_{\,L \to +\infty} || f - f_L || = 0$.

Based on the above theoretical foundations, SCN exhibits good universal approximation capability, along with fast learning speed, high real-time performance, strong generalization ability, and minimal reliance on manual intervention. The algorithmic flow of SCN is shown in Figure 6.

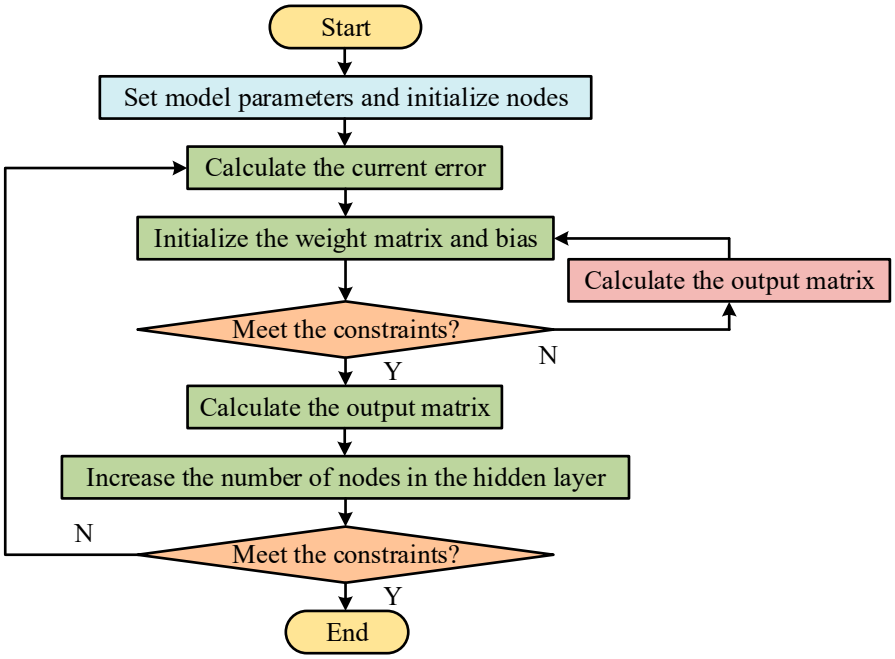


Figure 6. Algorithm flowchart of the stochastic configuration networks.

3.2. Sparrow Search Algorithm

The performance of SCN is influenced by the settings of hyperparameters. During the construction process, the initialization of weights and biases for candidate layer nodes depends on the scaling factor λ, while the computation of inequality constraints in the supervised mechanism depends on the regularization parameter γ. Therefore, the input weights and biases of hidden layer nodes are affected by λ and γ. To enhance the effectiveness of SCN, it is crucial to identify optimal parameters to maximize network performance and optimize the network structure. SSA is a swarm intelligence-based optimization algorithm inspired by the foraging behavior of sparrows, which simulates the cooperation and competition within sparrow populations during foraging to solve various optimization problems, featuring strong search capability, fast convergence, and high robustness. The specific optimization process of SSA can be described as follows:

A population X composed of n sparrows.

$$X = \begin{bmatrix} x_{1,1} & x_{1,2} & \cdots & x_{1,d} \\ x_{2,1} & x_{2,2} & \cdots & x_{2,d} \\ \vdots & \vdots & \vdots & \vdots \\ x_{n,1} & x_{n,2} & \cdots & x_{n,d} \end{bmatrix} \tag{12}$$

where n denotes the number of sparrows, and d denotes the dimensionality of the variables.

Discoverers with higher fitness obtain food preferentially during the search process, and they are responsible for locating food sources and guiding the movement of the entire population. The position update of discoverers is given as:

$$X_{i,j}^{t+1} = \begin{cases} X_{i,j}^{t} \mathrm{e}^{\left(\frac{-i}{\alpha T}\right)}, R_2 < S_T \\ X_{i,j}^{t} + QL, R_2 \geq S_T \end{cases} \tag{13}$$

where t denotes the current iteration number. $X_{i,j}^{t}$ denotes the position of the i-th sparrow in the j-th dimension at the t-th iteration, where $i, j = 1, 2, \ldots, N$. T denotes the maximum number of iterations. α is a random number in the range (0, 1]. R_2 denotes the alarm value and takes values in [0, 1]. S_T denotes the safety threshold and takes values in [0.5, 1]. Q is a random number following a normal distribution. L denotes $1 \times d$ matrix with all elements equal to 1.

When $R_2 < S_T$, it indicates that there are no predators nearby, and the discoverers enter a wide range search mode. When $R_2 \geq S_T$, it indicates the presence of danger in the vicinity, the discoverers issue an alarm, and all sparrows rapidly move to other safe regions.

During the foraging process, joiners move toward better food sources, and their position update is described as:

$$X_{i,j}^{t+1} = \begin{cases} Q\mathrm{e}^{\left(\frac{X_{worst}^{t} - X_{i,j}^{t}}{i^2}\right)}, i > \frac{n}{2} \\ X_{P}^{t+1} + \left| X_{i,j}^{t} - X_{P}^{t+1} \right| A^{+} L, i \leq \frac{n}{2} \end{cases} \tag{14}$$

where $A^{+} = A^{\mathrm{T}}(AA^{\mathrm{T}})^{-1}$, X_P denotes the best position occupied by the discoverers. X_{worst} denotes the current global worst position. A is $1 \times d$ matrix whose elements are randomly assigned as either 1 or -1.

It is assumed that 10% to 20% of the sparrow population becomes aware of danger. Sparrows that perceive danger exhibit antipredation behavior and move toward safe regions. The position update of vigilant sparrows is described as:

$$X_{i,j}^{t+1} = \begin{cases} X_{best}^{t} + \beta \left| X_{i,j}^{t} - X_{best}^{t} \right|, f_i > f_g \\ X_{i,j}^{t} + K \left(\frac{\left| X_{i,j}^{t} - X_{worst}^{t} \right|}{(f_i - f_w) + \varepsilon} \right), f_i = f_g \end{cases} \tag{15}$$

where X_{best} denotes the current global best position, and β denotes the step size control parameter and follows a normal distribution with zero mean and unit variance. K represents the movement direction of a sparrow and is a random number within the interval $[-1, 1]$. f_i denotes the fitness value of the current sparrow individual, f_g denotes the global best fitness value, f_w denotes the global worst fitness value. ε is a small constant introduced to avoid division by zero.

When $f_i > f_g$, the sparrow is located at the edge of the population, and X_{best} represents the position of the population center, which is considered safe. When $f_i = f_g$, the sparrow

located in the middle of the population becomes aware of danger and needs to move closer to other sparrows.

By iteratively updating according to the above steps, the fitness of the population continuously improves, and the optimal parameters are obtained after a certain number of iterations.

3.3. SSA-SCN

To improve the prediction accuracy and efficiency of SCN for battery capacity, the sparrow search algorithm is employed to optimize the hyperparameters of the stochastic configuration network model, namely the scaling factor λ and the regularization coefficient γ. The specific procedure of SSA-SCN can be described as follows:

Step 1: Set the number of sparrows n and the maximum number of iterations T, determine the maximum number of hidden layer nodes $L_{\max}$, the maximum number of candidate nodes $T_{\max}$, the tolerance error ε, and the hyperparameter ranges $\lambda \in [0.5, 200]$ and $\gamma \in [0.9, 0.9999]$.

Step 2: Construct and train the model. SCN is trained using the initial hyperparameters to obtain the initial fitness value as a baseline for optimization and mean square error (MSE) is adopted as the fitness function to evaluate the optimization performance of SSA-SCN. MSE defined in Equation (16).

$$\mathrm{MSE} = \frac{1}{n}\sum_{i=1}^{n}(y - \hat{y})^2 \tag{16}$$

where n is the number of samples, $\hat{y}$ is the predicted value, and y is the actual value.

Step 3: Execute the SSA. By continuously updating the positions of sparrows to improve fitness, the scaling factor λ and the regularization coefficient γ of SCN are optimized.

Step 4: Check whether the iteration number reaches the maximum value T or the fitness error satisfies the predefined threshold ε. If either condition is met, the iteration is terminated.

Step 5: Select the sparrow individual with the highest fitness obtained during SSA iterations, take its position parameters as the scaling factor λ and regularization coefficient γ of SCN, and construct SSA-SCN prediction model using the optimized hyperparameters.

SSA conducts dual-parameter collaborative optimization on λ and γ of SCN. It achieves a combined mechanism of structural adaptive growth and global parameter optimization. Compared with other optimization algorithms, Particle Swarm Optimization has a fast convergence speed but is prone to getting stuck in local optima. Genetic Algorithm has the advantage of strong global optimization ability but has the drawback of slow convergence. In contrast, SSA method can achieve a balance between global and local optimization, and it has stable convergence and fast speed. SSA-SCN adopts a single hidden layer structure and uses generalized inverse to solve without backpropagation. The low-dimensional feature input scenario is more compatible with the real-time RUL scenario of lithium-ion batteries.

The pseudocode is as follows (Algorithm 1):

Algorithm 1. SSA-SCN Algorithm

Input: battery features and historical capacity data
Output: battery capacity
1: Initialize parameters, including the sparrow population size n, the maximum iteration number T, the maximum number of hidden layer nodes $L_{\max}$, the maximum number of candidate nodes $T_{\max}$, the tolerance error ε, the scaling factor $\lambda \in [0.5, 200]$, and the regularization coefficient $\gamma \in [0.9, 0.9999]$.
2: Initialize the sparrow positions $X = \{x_1, x_2, \ldots, x_n\}$.
3: Construct and train the initial SCN model.
4: for $i = 1$ to n do
5: Randomly initialize λ and γ, train the SCN model using λ and γ, and compute the fitness value $f(x_i)$.
6: end for
7: Record the current best position X_{best} and its fitness value $f(X_{best})$.
8: Optimize SCN hyperparameters using SSA.
9: for $t = 1$ to T do
10: Update the positions of the discoverers.
11: Update the positions of the joiners.
12: Update the positions of vigilant sparrows.
13: if $f(X_{best}) \leq \varepsilon$
14: end for
15: Construct the final SCN model using the optimized parameters.
16: Use the trained SCN model to predict battery capacity.

4. Lithium-Ion Battery RUL Prediction Based on the SSA-SCN Method

To systematically evaluate the effectiveness of the proposed method for lithium-ion battery RUL prediction, this study establishes an RUL prediction framework based on health feature extraction and data-driven modeling. First, historical information including capacity, voltage, and current is extracted from full life cycle charge and discharge experimental data. To address the non-stationarity and capacity regeneration phenomena in the capacity sequence, multidimensional HFs that characterize battery degradation are constructed from key charge and discharge stages, and Pearson and Spearman correlation analyses are applied to quantitatively screen HFs to ensure strong correlation with capacity degradation. On this basis, a prediction model is constructed using the selected HFs to model and train battery capacity, and online capacity estimation is achieved during the prediction stage. When the predicted capacity reaches the predefined FT, the battery RUL is estimated accordingly to complete the prediction process. The overall framework of the proposed prediction process is shown in Figure 7.

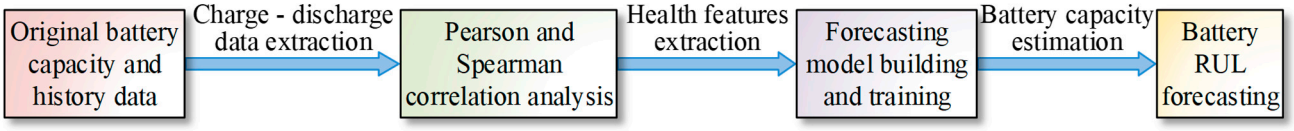


Figure 7. Flowchart of the RUL prediction process.

4.1. Analysis and Discussion of Prediction Results

Variations in capacity directly characterize the degree of battery degradation during charge and discharge cycles. Therefore, battery performance degradation is evaluated through capacity to predict the RUL of lithium-ion batteries. To verify the performance of

the proposed method for lithium-ion battery RUL prediction, the battery degradation data from the NASA dataset described in Section 2.1 are used for testing, and the prediction results of SSA-SCN are compared with those obtained by SVR, LSTM, and SCN methods. Forty percent of the data from four test batteries are used as training samples, corresponding to 68 cycles for B0005, B0006, and B0007, and 52 cycles for B0018. When the first 68 charge and discharge cycles of the lithium-ion battery are used as training samples, RUL prediction results obtained by SVR, LSTM, SCN, and the proposed method are shown in Figure 8, and the prediction errors of the four methods are listed in Table 5.

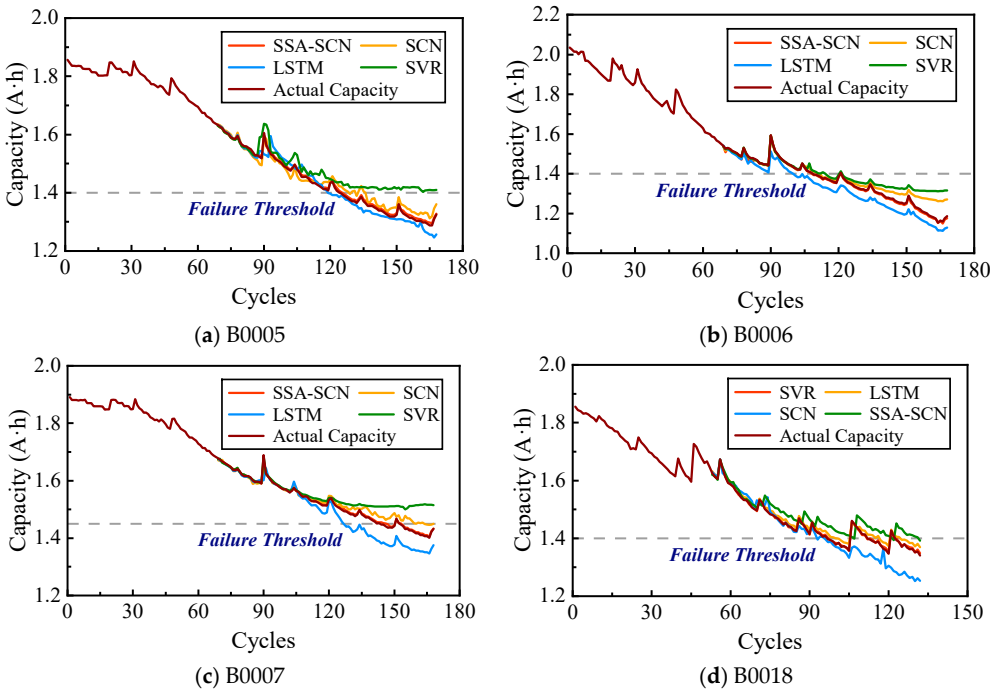


Figure 8. RUL prediction results with 40% battery training data.

Table 5. RUL prediction errors with 40% training set.

Battery	Start	Method	RUL	PRUL	Er	P_{Er}
B0005	69	SVR	56	-	-	-
		LSTM		50	6	10.71%
		SCN		60	4	7.14%
		SSA-SCN		57	1	1.79%
B0006	69	SVR	40	46	6	15.00%
		LSTM		31	9	22.50%
		SCN		43	3	7.50%
		SSA-SCN		40	0	0
B0007	69	SVR	75	-	-	-
		LSTM		58	17	22.67%
		SCN		91	16	21.33%
		SSA-SCN		78	3	4.00%
B0018	53	SVR	44	54	10	22.73%
		LSTM		40	4	9.09%
		SCN		48	4	9.09%
		SSA-SCN		45	1	2.27%

In Table 5, PRUL denotes the predicted RUL, RUL denotes the true value, and Er represents the absolute error between PRUL and RUL. When the lithium-ion battery

capacity degrades to FT, the errors, P_{Er} and Er, between the actual number of cycles and the predicted number of cycles are defined as follows.

$$\mathrm{Er} = |\mathrm{PRUL} - \mathrm{RUL}| \tag{17}$$

$$P_{\mathrm{Er}} = \frac{|\mathrm{PRUL} - \mathrm{RUL}|}{\mathrm{RUL}} \times 100\% \tag{18}$$

As shown in Table 5, compared with SVR, LSTM, and SCN, the SSA-SCN method yields smaller Er and P_{Er} values for batteries B0005 and B0007. "-" indicates that the predicted capacity has not reached FT and thus RUL cannot be calculated. As shown in Figure 8, RUL predicted by SVR does not reach FT and is therefore denoted by "-". For example, for B0006, the Er and P_{Er} values obtained by LSTM are 6 and 15%, respectively, those of SVR are 9 and 22.5%, those of SCN are 3 and 7.5%, while both Er and P_{Er} obtained by SSA-SCN are 0. For B0007, RUL predicted by SVR does not reach FT, the Er values obtained by LSTM and SCN are 17 and 16, respectively, whereas the Er obtained by the SSA-SCN method is only three cycles. As shown in Table 5, the prediction error of SSA-SCN is within three cycles, and zero error is achieved in some cases. In summary, the SSA-SCN method demonstrates relatively higher prediction accuracy for lithium-ion battery RUL.

To further analyze the prediction accuracy of the four methods, the mean absolute error (MAE), root mean square error (RMSE), and mean absolute percentage error (MAPE) obtained from the four methods are adopted as evaluation metrics for statistical analysis, and the definitions of MAE, RMSE, and MAPE are given as follows.

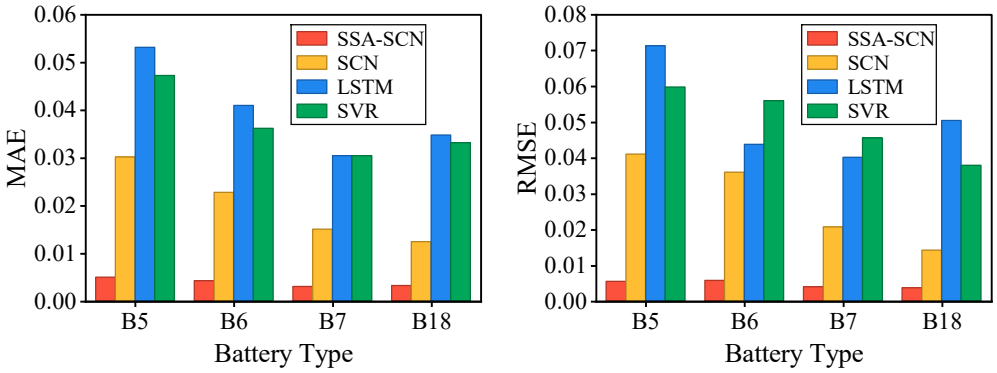
$$\mathrm{MAE} = \frac{1}{n}\sum_{i}^{n}|\hat{y}_i - y_i| \tag{19}$$

$$\mathrm{RMSE} = \sqrt{\frac{1}{n}\sum_{i}^{n}(\hat{y}_i - y_i)^2} \tag{20}$$

$$\mathrm{MAPE} = \frac{1}{n}\sum_{i=1}^{n}\frac{|y_i - \hat{y}_i|}{y_i} \tag{21}$$

where $\hat{y}_i$ denotes the predicted capacity, and y_i denotes the actual capacity.

To ensure the statistical reliability and objectivity of the experimental results, all the models in this paper were independently run multiple times, and statistical analysis was conducted on various evaluation indicators. The presented experimental results are the average values of multiple experiments, thereby effectively reducing the influence of random factors on the results of a single experiment. As shown in Figure 9, the errors obtained by the SSA-SCN method are smaller than those of the other three methods. For B0005, the MAE and RMSE values of the SVR are 0.0473 and 0.0598, respectively, while those of the SSA-SCN method are 0.0050 and 0.0055, respectively, which are approximately one-ninth of SVR results. Repeated experiments have shown that the proposed SSA-SCN method maintains stable prediction accuracy under different operating conditions, verifying the stability and repeatability of its results.



(**a**) MAE (**b**) RMSE

Figure 9. Evaluation metrics of RUL prediction with 40% training set.

4.2. Comparison Experiments and Analysis

Three representative machine learning methods, denoted as M2 [18], M3 [37], and M4 [38], are selected as benchmarks against the proposed SSA-SCN method (M1), corresponding to the deep learning approach CNN-Attention-SMA-GPR (M2), the intelligence optimized hybrid model AE-CNN-TCN-BiLSTM-Attention (M3), and the Bayesian linear regression-based method BLR-FR (M4), thereby covering the main data-driven approaches for battery RUL estimation. Figure 10 presents the RUL prediction results for four NASA batteries when the first 50% of cycle data are used as training samples. The experimental results show that the SSA-SCN method effectively mitigates the impact of battery capacity regeneration on RUL prediction. The sudden change range of capacity in the red box area of the figure clearly shows a nonlinear characteristic. M1 can effectively track the peak of capacity regeneration and its subsequent decay trend, while other models generally have problems such as underestimated peaks, delayed responses or excessive smoothing near the regeneration point. After precise processing by the proposed method, the predicted results are closer to the true RUL to a certain extent. In contrast, the benchmark models exhibit noticeable fluctuations at different stages. To provide a more intuitive analysis of RUL prediction results, the error distribution in Figure 11 further statistically analyzes the prediction accuracy of M1 to M4. It can be observed that the boxplot distribution of the proposed method M1 exhibits a highly concentrated pattern. The mean error remains nearly stable around zero, indicating that the prediction results were stable with relatively small deviations. In contrast, the errors from M2 to M4 are relatively scattered, showing obvious positive or negative bias, and the degree of error dispersion is greater. Some batteries exhibit wide probability density bands and significant abnormal behaviors. These results indicate that SSA-SCN still maintains good robustness and consistency under complex degradation trajectories and nonlinear changes. Its statistical distribution performance is consistent with the previous error index analysis results.

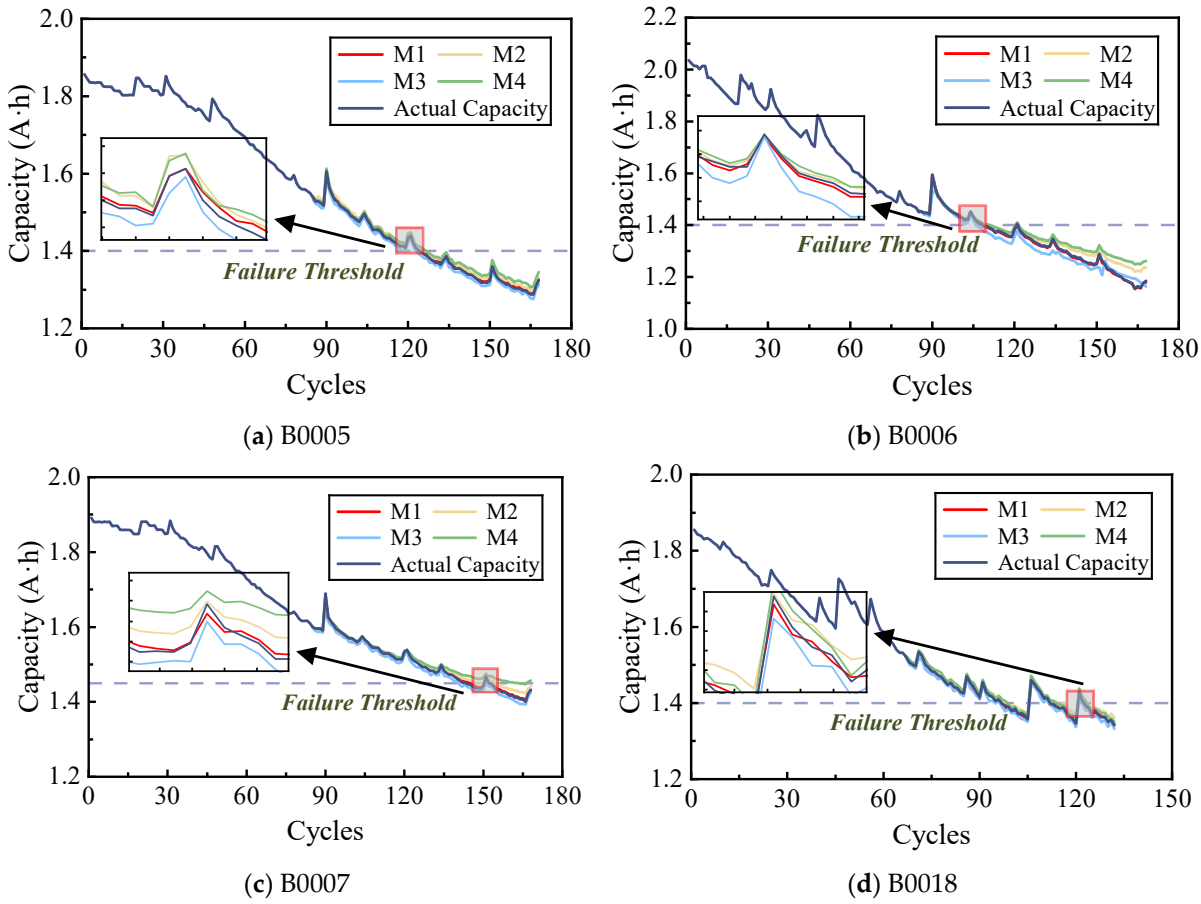


Figure 10. Comparative experiments on the NASA dataset with 50% training set.

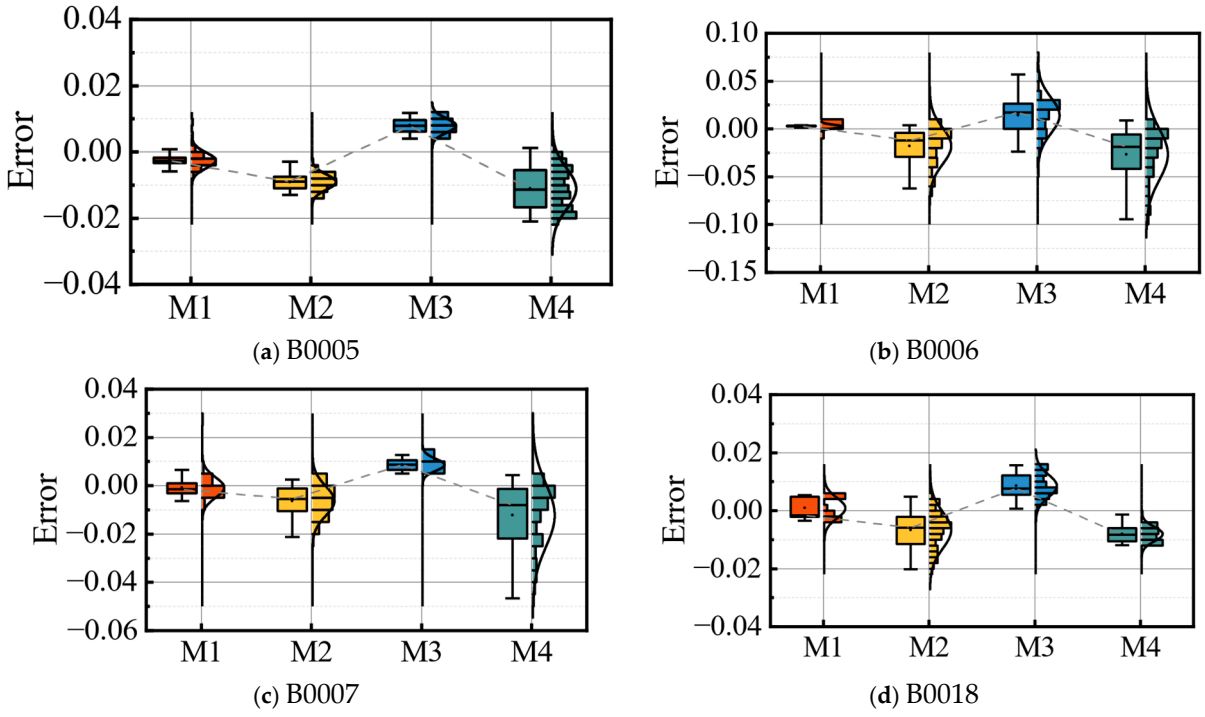


Figure 11. Error distribution of comparison methods.

As shown in Table 6, RMSE of M1 is lower than that of M2, M3, and M4 by 0.0097, 0.0089, and 0.0155, respectively. MAE of M1 is lower than that of M2, M3, and M4 by

0.0074, 0.0081, and 0.0097, respectively. MAPE of M1 is lower than that of M2, M3, and M4 by 0.0057, 0.0059, and 0.0090, respectively. This indicates that the proposed method can effectively reduce the adverse impact of capacity regeneration in the dataset on prediction accuracy. This advantage mainly arises from the global optimization capability of SSA for SCN key hyperparameters and the efficient approximation of nonstationary degradation features by SCN during incremental modeling, enabling the model to accurately capture the dominant capacity evolution trend without relying on complex decomposition or deep architectures.

Table 6. Evaluation metrics of RUL prediction for comparison methods with 50% training set.

Battery	Method	RMSE	MAE	MAPE	Battery	Method	RMSE	MAE	MAPE
B0005	M1	0.00346	0.00296	0.00213	B0007	M1	0.00426	0.00295	0.00195
	M2	0.00938	0.00910	0.00652		M2	0.00878	0.00684	0.00470
	M3	0.00825	0.00796	0.00570		M3	0.00901	0.00866	0.00578
	M4	0.01269	0.01115	0.00821		M4	0.01782	0.01263	0.00873
B0006	M1	0.00310	0.00283	0.00213	B0018	M1	0.00360	0.00328	0.00232
	M2	0.02593	0.01833	0.01474		M2	0.00919	0.00734	0.00528
	M3	0.02332	0.01944	0.01468		M3	0.00935	0.00852	0.00601
	M4	0.03760	0.02718	0.02181		M4	0.00845	0.00807	0.00570

4.3. Generalization Analysis

To further verify the performance of the model, the CALCE dataset is used for testing. The CALCE dataset originates from the Center for Advanced Life Cycle Engineering at the University of Maryland [39]. Four batteries, numbered as CS35, CS36, CS37, and CS38, are selected from the CS2 series, each with a nominal capacity of 1.1 A·h [40]. The experiments employ constant current constant voltage charging and constant current discharging protocols. The constant current charging current is 0.45 A with a cut-off voltage of 4.2 V. The constant current discharging current is 0.45 A with a cut-off voltage of 2.7 V. The rated capacity of the CS2 batteries is 1.1 A·h; therefore, FT is set to 0.88 A·h.

In this section, the first 30% of the cycle data are used as training samples. Meanwhile, to ensure fairness in comparison, all benchmark models adopt the same grouped features. Figure 12 shows RUL prediction results of models M1 to M4 for CALCE batteries CS35, CS36, CS37, and CS38. From the overall trend, all the batteries showed a significant acceleration of degradation in the middle and later stages. The capacity curve changed from a slow decline to a steep decline phase, demonstrating a strong nonlinear dynamic. It can be observed that M1 was able to effectively track the capacity evolution trend across the tested batteries. Especially near FT, its predicted curve showed good agreement with the actual capacity, without evident premature or delayed failure behavior. The result indicates that SSA-SCN still maintains good generalization and stability in cross-dataset verification, can effectively depict the phased nonlinear changes during the degradation process, and verifies the adaptability and engineering application potential of the proposed method under different data sources.

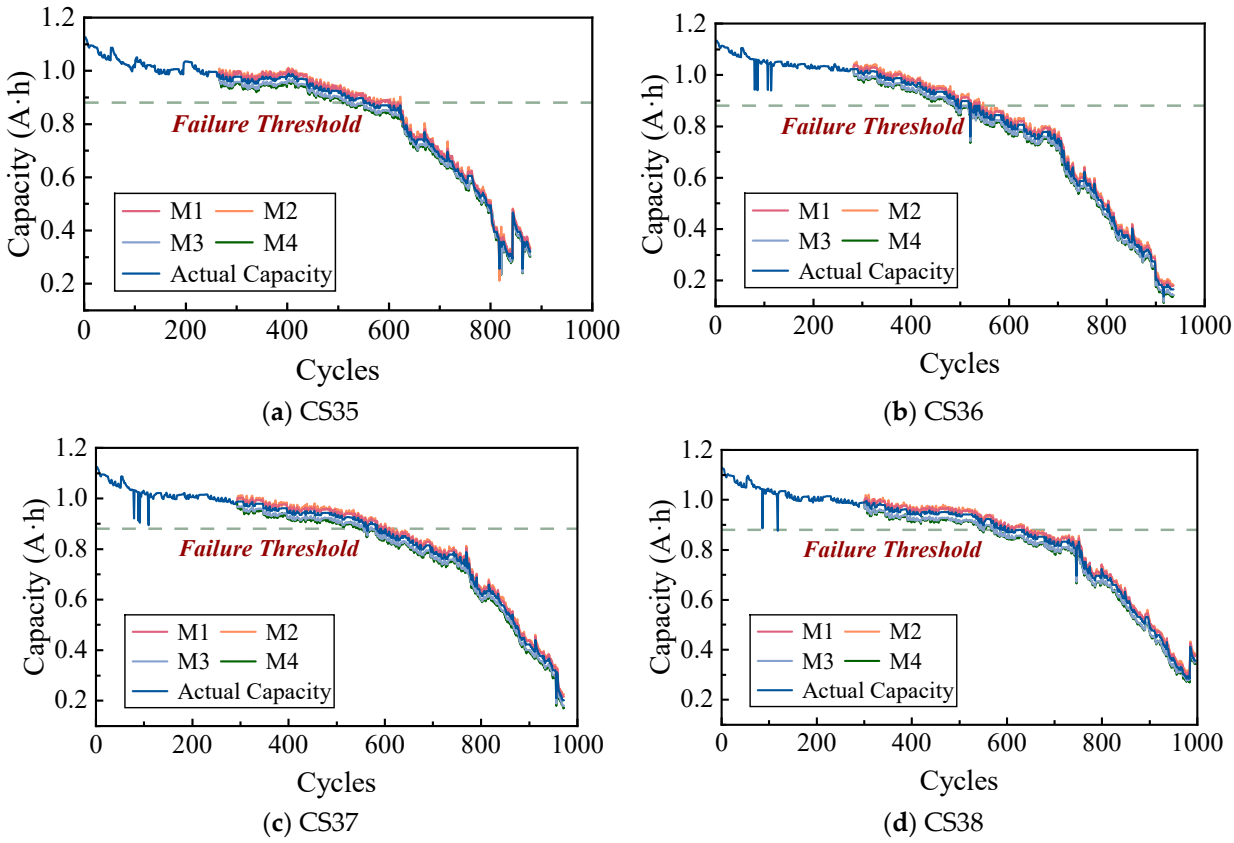
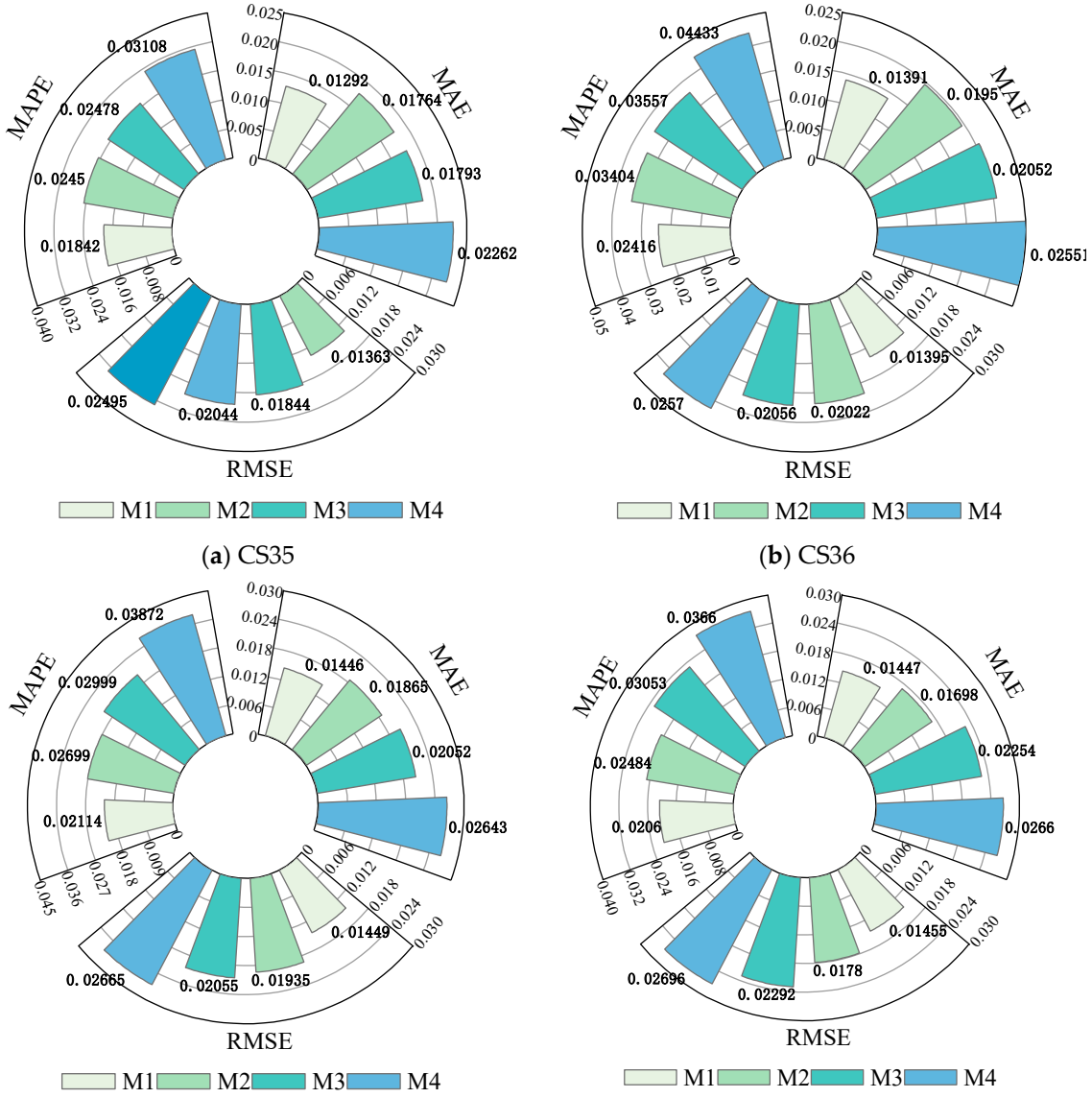


Figure 12. RUL prediction results on the CALCE dataset.

To ensure the fairness of the comparison of prediction times for different models, this study was conducted under a unified hardware and software environment. The experiments were all run on the platform of NVIDIA RTX 4060 GPU. The calculation times for different comparison methods are shown in Table 7. The proposed SSA-SCN (M1) exhibits the shortest prediction time among the compared methods for the CALCE batteries, with an average inference time of only 5.880 s. This is mainly attributed to its single hidden layer architecture, which avoids iterative backpropagation and deep temporal modeling. In contrast, deep hybrid models such as M3 exhibit significantly higher computational costs due to the integration of multiple deep modules. The computational time further indicates that SSA-SCN is more suitable for real-time battery remaining useful life prediction applications. Meanwhile, the evaluation metric results on the CALCE dataset shown in Figure 13 indicate that M1 exhibits clear advantages over the other methods. For the four batteries, the MAE, RMSE, and MAPE values of the proposed method are all below 0.015, 0.015, and 0.025, respectively. Compared with M2 to M4, the MAE is reduced by approximately 31%, 46%, and 81%, the RMSE by approximately 34%, 49%, and 84%, and the MAPE by approximately 31%, 43%, and 78%, respectively. Overall, Figure 13 further validates the proposed method from a multi-index statistical perspective in terms of its ability to generalize and its robustness in complex degradation environments. This is consistent with the previous results of error distribution and trend analysis, demonstrating the comprehensive advantages of SSA-SCN in the RUL prediction task.

Table 7. Prediction time of the comparison methods.

Method	CS35	CS36	CS37	CS38	Average
M1	5.238 s	5.601 s	6.224 s	6.456 s	5.880 s
M2	42.356 s	46.379 s	43.937 s	42.042 s	43.679 s
M3	118.077 s	121.546 s	119.283 s	120.908 s	119.953 s
M4	18.935 s	19.834 s	18.126 s	19.012 s	18.977 s



(**a**) CS35 (**b**) CS36

(**c**) CS37 (**d**) CS38

Figure 13. Distribution of RUL prediction errors for the CALCE dataset.

To further verify the generalization ability of the proposed method, two batteries from the NASA dataset, namely B0029 (test temperature of 43 °C) and B0053 (test temperature of 4 °C), were selected to supplement different operating conditions for further verification. Figure 14a,c show the capacity prediction curves of the two batteries under different comparison methods. Since neither of these two batteries reached the FT, the evaluation indicators were not used to statistically analyze the prediction results.

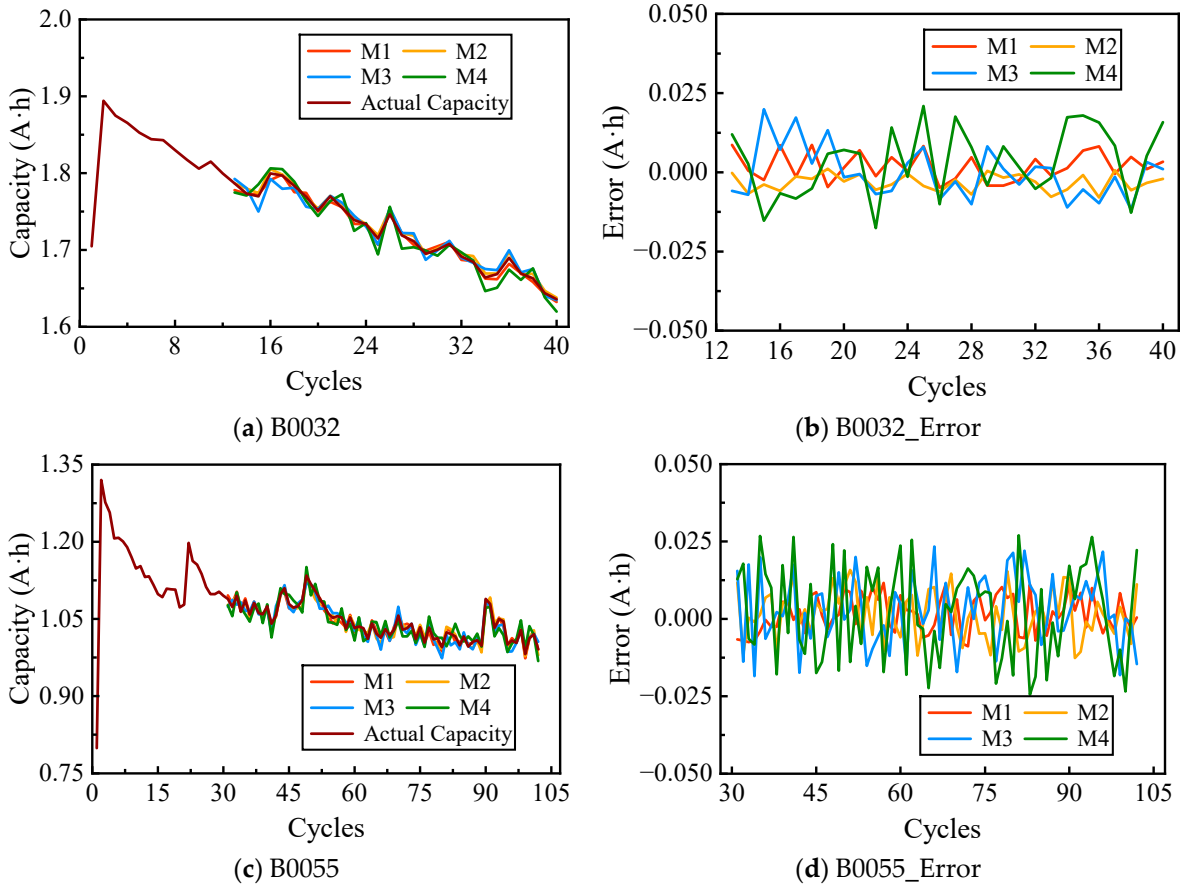


Figure 14. Generalization experiments of the NASA dataset under different test temperatures.

As shown in Figure 14b,d, the error value of the proposed method remains below 2% under both high temperature (43 °C) and low temperature (4 °C) conditions. Except for the room temperature environment (24 °C), this method demonstrates good adaptability under different working conditions.

5. Conclusions

Lithium-ion batteries are widely used in the energy storage field due to their superior performance, and accurate prediction of RUL can improve the safety and reliability of battery systems. In this study, the NASA and CALCE datasets are investigated, and features characterizing battery performance degradation together with cycle numbers are extracted from the charge–discharge stages to form HFs, while Pearson and Spearman correlation analyses are employed to examine their correlation with capacity and verify the feasibility of the extracted HFs. SSA that provides the optimal parameters for SCN is proposed, thereby enabling accurate RUL prediction of lithium-ion batteries, and the performance of the SSA-SCN method is validated using two battery degradation datasets through comparative analysis with other prediction methods. Therefore, the proposed prediction method can provide higher accuracy and timeliness for lithium-ion battery RUL prediction. In future work, the full life cycle of battery charge–discharge processes and variations in other features such as temperature during operation will be considered to achieve more accurate RUL prediction. The proposed method has not yet been validated on other batteries or under more complex operating conditions, and therefore further optimization is required for practical applications.

Future research will further incorporate dynamic conditions such as temperature variations and multi-rate charging and discharging to analyze the impact of temperature

coupling effects and load fluctuations on the stability of health characteristics and the accuracy of model predictions. It will also explore an extended framework that integrates environmental variables and operating conditions information in order to enhance the generalization ability and engineering applicability of the model in real-world scenarios. With the widespread application of large-scale energy storage systems, online adaptive and continuous learning can consider the sliding window incremental update mechanism, error-triggered local update strategies, and periodic background hyperparameter re-optimization. These methods need to be further enhanced in future engineering deployments to improve the model's ability to adapt to long-term drift problems.

Author Contributions: X.W.: Conceptualization, Writing—original draft. Z.G.: Supervision, Writing—review and editing. X.G.: Validation, Formal analysis. Y.N.: Visualization, Validation. Y.L.: Supervision, Validation. All authors have read and agreed to the published version of the manuscript.

Funding: This work was supported by the National Natural Science Foundation of China (62273243) and Liaoning Provincial Applied Basic Research Program (2025JH2/10130048).

Data Availability Statement: The original contributions presented in the study are included in the article, further inquiries can be directed to the corresponding author.

Conflicts of Interest: The authors declare no conflicts of interest.

References

1. Manfo, A. A Comprehensive Analysis of Material Revolution to Evolution in Lithium-ion Battery Technology. *Turk. J. Mater.* **2023**, *8*, 1–13.
2. Wei, M.; Ye, M.; Zhang, C.; Wang, Q.; Lian, G.; Xia, B. Integrating mechanism and machine learning based capacity estimation for $LiFePO_4$ batteries under slight overcharge cycling. *Energy* **2024**, *296*, 131208.
3. Theodore, M.; Şahin, E. Modeling and simulation of a series and parallel battery pack model in MATLAB/Simulink. *Turk. J. Electr. Power Energy Syst.* **2024**, *4*, 2–12.
4. Madani, S.; Shabeer, Y.; Allard, F.; Fowler, S.; Ziebert, C.; Wang, Z.; Panchal, S.; Chaoui, H.; Mekhilef, S.; Shi, X.; et al. A comprehensive review on lithium-ion battery lifetime prediction and aging mechanism analysis. *Batteries* **2025**, *11*, 127. [CrossRef]
5. Li, X.; Yu, D.; Byg, V.; Ioan, S. The development of machine learning-based remaining useful life prediction for lithium-ion batteries. *J. Energy Chem.* **2023**, *82*, 103–121.
6. Ahwiadi, M.; Wang, W. Battery health monitoring and remaining useful life prediction techniques: A review of technologies. *Batteries* **2025**, *11*, 31. [CrossRef]
7. Pan, D.; Li, H.; Wang, S. Transfer learning-based hybrid remaining useful life prediction for lithium-ion batteries under different stresses. *IEEE Trans. Instrum. Meas.* **2022**, *71*, 3501810. [CrossRef]
8. Lyu, Z.; Gao, R.; Chen, L. Li-ion battery state of health estimation and remaining useful life prediction through a model-data-fusion method. *IEEE Trans. Power Electron.* **2020**, *36*, 6228–6240. [CrossRef]
9. Song, K.; Hu, D.; Tong, Y.; Yue, X. Remaining life prediction of lithium-ion batteries based on health management: A review. *J. Energy Storage* **2023**, *57*, 106193. [CrossRef]
10. Tao, J.; Wang, S.; Cao, W.; Aninakwa, P.; Fernandez, C.; Guerrero, J. A comprehensive review of state-of-charge and state-of-health estimation for lithium-ion battery energy storage systems. *Ionics* **2024**, *30*, 5903–5927.
11. Koseoglou, M.; Tsioumas, E.; Panagiotidis, I.; Papagiannis, D.; Jabbour, N.; Mademlis, C. A lithium-ion battery equivalent circuit model based on a hybrid parametrization approach. *J. Energy Storage* **2023**, *73*, 109051. [CrossRef]
12. Wei, M.; Ye, M.; Zhang, C.; Lian, G.; Xia, B.; Wang, Q. Robust state of charge estimation of LiFePO4 batteries based on Sage_Husa adaptive Kalman filter and dynamic neural network. *Electrochim. Acta* **2024**, *477*, 143778. [CrossRef]
13. Du, Z.; Zuo, L.; Li, J.; Liu, Y.; Shen, H. Data-driven estimation of remaining useful lifetime and state of charge for lithium-ion battery. *IEEE Trans. Transp. Electrif.* **2021**, *8*, 356–367.
14. Keshun, Y.; Guangqi, Q.; Yingkui, G. Remaining useful life prediction of lithium-ion batteries using EM-PF-SSA-SVR with gamma stochastic process. *Meas. Sci. Technol.* **2023**, *35*, 015015. [CrossRef]
15. Elbarbary, S.; Hoskeri, A.; Javidparvar, A.; Alammar, M.; Rajakannu, A.; Manfo, A. Machine Learning Approach to the Possible Synergy Between Co-Doped Elements in the Case of $LiFePO_4$/C. *J. Alloys Compd.* **2025**, *1034*, 181316. [CrossRef]
16. Sun, Y.; Xie, H.; Diao, Q.; Xu, H.; Tan, X.; Fan, Y.; Wei, L. A novel SOH estimation method with attentional feature fusion considering differential temperature features for lithium-ion batteries. *IEEE Trans. Instrum. Meas.* **2024**, *73*, 3538911. [CrossRef]

17. Alsuwian, T.; Ansari, S.; Zainuri, M.; Ayob, A.; Hussain, A.; Lipu, M.; Alhawari, A.; Almawgani, A.; Almasabi, S.; Hindi, A. A review of expert hybrid and co-estimation techniques for SOH and RUL estimation in battery management system with electric vehicle application. *Expert Syst. Appl.* **2024**, *246*, 123123. [CrossRef]
18. Tian, A.; Yu, H.; Hu, Z.; Wang, Y.; Wu, T.; Jiang, J. A novel remaining useful life prediction method based on CNN-Attention combined with SMA-GPR. *Energy* **2025**, *321*, 135233. [CrossRef]
19. Jia, S.; Ma, B.; Guo, W.; Li, Z. A sample entropy based prognostics method for lithium-ion batteries using relevance vector machine. *J. Manuf. Syst.* **2021**, *61*, 773–781. [CrossRef]
20. Sun, C.; Lu, T.; Li, Q.; Liu, Y.; Yang, W.; Xie, J. Predicting the Future Capacity and Remaining Useful Life of Lithium-Ion Batteries Based on Deep Transfer Learning. *Batteries* **2024**, *10*, 303. [CrossRef]
21. Zhou, Y.; Wang, S.; Xie, Y.; Shen, X.; Fernandez, C. Remaining useful life prediction and state of health diagnosis for lithium-ion batteries based on improved grey wolf optimization algorithm-deep extreme learning machine algorithm. *Energy* **2023**, *285*, 128761.
22. Wang, Y.; Wang, S.; Fan, Y.; Xie, Y.; Hao, X.; Guerrero, J. High-precision collaborative estimation of lithium-ion battery state of health and remaining useful life based on call activation function library-long short term memory neural network algorithm. *J. Energy Storage* **2024**, *83*, 110749. [CrossRef]
23. Gomez, W.; Wang, F.; Chou, J. Li-ion battery capacity prediction using improved temporal fusion transformer model. *Energy* **2024**, *296*, 131114. [CrossRef]
24. Zhang, Z.; Liu, X.; Dong, X.; Jiang, P.; Zhang, R.; Zhang, C.; Shao, J.; Xie, Y.; Zhang, Y.; Liu, X.; et al. A Hybrid RUL Prediction Framework for Lithium-ion Batteries Based on EEMD and KAN-LSTM. *Batteries* **2025**, *11*, 348. [CrossRef]
25. Wang, G.; Sun, L.; Wang, A.; Jiao, J.; Xie, J. Lithium battery remaining useful life prediction using VMD fusion with attention mechanism and TCN. *J. Energy Storage* **2024**, *93*, 112330. [CrossRef]
26. Duan, C.; Cao, H.; Liu, F.; Li, X.; Duan, X.; Sheng, B. Lithium-ion batteries remaining useful life prediction using a parallel BILSTM-MHA neural network based on a CEEMDAN module. *Int. J. Adv. Manuf. Technol.* **2025**, *137*, 3359–3386. [CrossRef]
27. Liu, L.; Sun, W.; Yue, C.; Zhu, Y.; Xia, W. Remaining useful life estimation of lithium-ion batteries based on small sample models. *Energies* **2024**, *17*, 4932. [CrossRef]
28. Lixin, E.; Wang, J.; Yang, R.; Wang, C.; Li, H.; Xiong, R. A physics-informed neural network-based method for predicting degradation trajectories and remaining useful life of supercapacitors. *Green Energy Intell. Transp.* **2025**, *4*, 100291.
29. Wang, F.; Zhai, Z.; Zhao, Z.; Di, Y.; Chen, X. Physics-informed neural network for lithium-ion battery degradation stable modeling and prognosis. *Nat. Commun.* **2024**, *15*, 4332. [CrossRef] [PubMed]
30. Zhang, J.; Jiang, Y.; Li, X.; Huo, M.; Luo, H.; Yin, S. An adaptive remaining useful life prediction approach for single battery with unlabeled small sample data and parameter uncertainty. *Reliab. Eng. Syst. Saf.* **2022**, *222*, 108357. [CrossRef]
31. Marghichi, M.; Loulijat, A.; Hantati, I. Variable recursive least square algorithm for online battery equivalent circuit model parameters identification for electric vehicles. *Electr. Eng.* **2024**, *106*, 2425–2445. [CrossRef]
32. Barcellona, S.; Ribera, M.; Fedele, E.; Franzese, P.; Piegari, L.; Codecasa, L.; Iannuzzi, D. State of Health Estimation of Lithium Cobalt Oxide Batteries Based on ARX Identification Across Different Temperatures. *Batteries* **2025**, *12*, 2. [CrossRef]
33. Cheng, Y.S. Identification of parameters for equivalent circuit model of Li-ion battery cell with population based optimization algorithms. *Ain Shams Eng. J.* **2024**, *15*, 102481. [CrossRef]
34. Saha, B.; Goebel, K. Battery Data Set: NASA Ames Prognostics Data Repository [EB/OL]. Available online: http://ti.arc.nasa.gov/pro-ject/prognostic-data-repository (accessed on 17 January 2007).
35. Yao, F.; He, W.; Wu, Y.; Ding, F.; Meng, D. Remaining useful life prediction of lithium-ion batteries using a hybrid model. *Energy* **2022**, *248*, 123622. [CrossRef]
36. Wang, D.; Li, M. Stochastic configuration networks: Fundamentals and algorithms. *IEEE Trans. Cybern.* **2017**, *47*, 3466–3479. [CrossRef]
37. Li, F.; Yang, D.; Li, J.; Wang, S.; Wu, C.; Li, M.; Li, C.; Han, P.; Qian, H. Remaining Useful Life Estimation of Lithium-Ion Batteries Using Alpha Evolutionary Algorithm-Optimized Deep Learning. *Batteries* **2025**, *11*, 385. [CrossRef]
38. Bai, J.; Huang, J.; Luo, K.; Yang, F.; Xian, Y. A feature reuse based multi-model fusion method for state of health estimation of lithium-ion batteries. *J. Energy Storage* **2023**, *70*, 107965. [CrossRef]
39. Ke, Y.; Long, M.; Yang, F.; Peng, W. A Bayesian deep learning pipeline for lithium-ion battery SOH estimation with uncertainty quantification. *Qual. Reliab. Eng. Int.* **2024**, *40*, 406–427. [CrossRef]
40. He, W.; Williard, N.; Osterman, M.; Pecht, M. Prognostics of lithium-ion batteries based on Dempster–Shafer theory and the Bayesian Monte Carlo method. *J. Power Sources* **2011**, *196*, 10314–10321. [CrossRef]

Disclaimer/Publisher's Note: The statements, opinions and data contained in all publications are solely those of the individual author(s) and contributor(s) and not of MDPI and/or the editor(s). MDPI and/or the editor(s) disclaim responsibility for any injury to people or property resulting from any ideas, methods, instructions or products referred to in the content.